Modeling and Transient Synchronization Stability Analysis for PLL-Based Renewable Energy Generator Considering Sequential Switching Schemes

Jinxin Pei, Jun Yao, *Member, IEEE*, Yuan Liu, Shiyue Chen, Peng Sun, and Sen Huang

***Abstract*—The synchronization characteristics of phase-locked loop (PLL) based renewable energy generators (REG) are considerably sensitive to the grid condition and the inner sequential switching actions of their control system, especially suffered from grid faults. In this article, the general output characteristics of REG systems are investigated considering the nonlinear behaviour of PLL. In addition, general sequential switching control schemes for the entire grid fault process are introduced. Then, to physically determine and theoretically analyze the transient synchronization stability of REG systems, the synchronization model of a REG system for different fault stages is built and presented in the form of rotor swing equations, which are similar to those of a synchronous generator (SG). The proposed model was able to deduce the characteristics of virtual torque, virtual inertia, and virtual damping coefficient of the REG system, and identify the coupling relationship between the angular frequency/magnitude states of the terminal voltage of the REG system during the synchronization process. Thus, the synchronization stability criteria were proposed based on those of the SG, in which the transient instability phenomenon and mechanism for different fault stages is physically explained by the deduced equal area criteria. Finally, the analysis was verified by simulations and experiments.**

***Index Terms*—Renewable energy generator (REG), rotor swing equation, sequential switching actions, synchronization stability.**

NOMENCLATURE

$\omega_0, \omega_g, \omega_b$	Nominal grid angular velocity, grid voltage vector's angular velocity, and base value of angular velocity, respectively.
$\theta_{PLL}, \omega_{PLL}$	Output angle and angular frequency of PLL, respectively.
$\boldsymbol{U_t}, \boldsymbol{I}$	Terminal voltage and output current of REG system, respectively.
R_g, L_g	Equivalent resistance and inductance of the transmission line, respectively.
k_{pp}, k_{ip}	PI coefficients of the PLL.
C_f, L_f	Filter capacitor and filter inductance, respectively.
U_{dc}	Direct current (dc) link voltage.
T_v, J_v, D_v	Virtual torque, inertia, and damping coefficient, respectively.

SUBSCRIPTS

d/q	*d/q*-axis components.
m	Maximum value.
b	Base value.
n, f, rec	Values in prefault, low voltage ride through (LVRT), and postfault grid condition, respectively.

SUPERSCRIPTS

$*$	Instruction value.

Manuscript received November 16, 2020; revised April 7, 2021 and June 28, 2021; accepted August 2, 2021. Date of publication August 10, 2021; date of current version October 15, 2021. This work was supported in part by the Joint Research Fund in Smart Grid under Grant U1966208 under cooperative agreement between the National Natural Science Foundation of China and State Grid Corporation of China, in part by the National Natural Science Foundation of China under Grant 51977019, in part by the 111 Project of China under Grant B18062, and in part by the State Grid Chongqing Electric Power Company under Grant 52202319004G. *(Corresponding author: Jun Yao.)*

The authors are with the State Key Laboratory of Power Transmission Equipment and System Security and New Technology, School of Electrical Engineering, Chongqing University, Chongqing 400044, China (e-mail: peijinxindoc@163.com; topyj@163.com; yuanliu18@cqu.edu.cn; csy_chenshiyue@163.com; wdfasfe@qq.com; huangsenwarm@163.com).

Color versions of one or more figures in this article are available at https://doi.org/10.1109/TPEL.2021.3103017.

Digital Object Identifier 10.1109/TPEL.2021.3103017

I. INTRODUCTION

THE synchronization mechanism of the current mainstream renewable energy generators (REGs) is based on its control structure, and determined by phase-locked loop (PLL) technology, which is considerably different from that of synchronous generators (SGs) [1]–[3]. This implies that REG dominated local power system face significantly changes in enabling transient synchronization stability under grid faults. As REGs have been increasingly adopted, the disconnection of REG systems from the utility grid under abnormal grid condition must be avoided because of the considerable power generation deficit [4], [5]. Consequently, low voltage ride through (LVRT) capability in REG systems is proposed in grid codes [6], [7]. However, the transient stability of PLL-based REG systems still experiences various challenges, which has generated concerns [8]–[10].

According to the grid codes, the REG system must remain grid-connected in a control state during LVRT, which corresponds to injecting reactive current in response to the grid codes. However, many studies identified a small signal instability risk

for REG systems during LVRT because of the interaction between the power grid and system controllers [11]–[13].

Furthermore, the large disturbance stability of REG systems has gained increasing attention in recent years [14]. Some innovative studies demonstrate the existence of a loss of synchronization (LOS) phenomenon in REG systems, which originates from the inability of PLLs to remain synchronized with the grid during LVRT [15]–[18]. In [15], a stability criterion focused on the existence of equilibrium points was studied for a REG system during deep voltage sags. In [16], the mechanism of LOS was explained by providing deep insights into low-frequency nonlinear behaviors of PLL. The results showed that the interaction between the REG output current and the transmission line impedance may result in the lack of equilibrium points in the grid-connected REG system. In [17], a creative voltage-vector-triangle graphic method was proposed to study both the criterion for the existence of equilibrium points and the LOS evolution process of the grid-connected REG system during LVRT. In [18], the transient instability response of the doubly fed induction generator (DFIG) based single-machine infinite bus system by the transient energy function method was studied. However, these studies assumed that the control loops of the system were perfect and ideal and mainly focused on the existence of equilibrium points for REG systems.

Although the presence of equilibrium points is a necessary condition for the transient stability of an REG system, the effect of transient behaviors on the synchronization stability of REG systems is rarely considered [14]. Both the dynamic performance of the system controllers and the interaction between REG and power grid may significantly affect the transient properties of the REG system, thus causing the LOS phenomenon even if there is an equilibrium point. Geng *et al.* [19], [20] explored transient synchronization stability of REG systems by considering the controller dynamics. Particularly, Wu and Wang [21] recently reported that the PLL can be regarded as a second-order nonlinear swing equation to REG systems during LVRT. Moreover, Wu and Wang [21], [22] developed a new perspective by using the phase portrait method, which reveals the impact of the PLL on the transient stability of REG systems and deduces the expression of the PLL damping ratio. The studies show that a high PLL damping ratio can improve the transient stability of REG systems. In addition, the limited overcurrent capability of power converters requires the use of current limiting control [23], which imposes another constraint on the transient stability behavior of REG systems [24]. Moreover, some studies have applied Lyapunov's direct method to study the transient stability of PLL-synchronized REG systems [20], [21], but the damping term has not yet been considered.

To avoid the LOS phenomenon for the voltage source converter (VSC) during severe grid fault, Göksu *et al.* [15] and He *et al.* [20] proposed adaptively injecting active current based on the terminal frequency, and Pei *et al.* [17] indicated that the REG system has the highest margin when the ratio of the active/reactive current instruction equals R_g/X_g. All the mentioned studies on stability of REG systems focus on the period of LVRT. In particular, many system behaviors during other fault stages are rarely considered, such as initial state, detection delay, and sequential control switching actions [25], [26]. The transient stability of the REG system is seldom systematically studied from the viewpoint of the entire fault process, without focusing only on the sequential control switching actions of REGs. In practice, the sequential switching actions of the control system must be triggered to respond to the variation of grid condition, particularly during the entire fault process, which further affects the synchronization behaviors [18], [25], [26].

Consequently, this article aims to physically analyze the transient synchronization stability of PLL-based REG systems and systematically improve the instability criteria from the perspective of the entire grid fault process. The main contributions of this article are presented as follows.

1) The transient responses of PLL-based REG systems are divided into five stages in the entire grid fault process according to its sequential control switching schemes. Furthermore, considering the nonlinear behaviors of PLL and *d*/*q*-axis components of terminal voltage in each grid fault stage, the transient synchronization characteristics of REG systems for different stages are represented by the deduced equivalent rotor swing equations, whose form is similar to that of SG.
2) Based on the deduced equivalent rotor swing equations of the REG system for different stages, by analyzing the defined virtual prime mover torque and the actual output torque, this article essentially revealed the coupled driving relationship between the angular frequency/magnitude states of the REG system terminal voltage. Moreover, the transient synchronization characteristics of the REG system are also analyzed according to the defined synchronization parameters, involving the equivalent power angle (EPA), virtual inertia, and virtual damping coefficient.
3) Based on the abovementioned analysis, the transient instability phenomenon and mechanism for the entire grid fault is physically explained by deduced equal area criteria (EAC), which consider system transient behaviors, control parameters, sequential control switching actions, and detection delay. This makes the transient synchronization stability criterion of the REG system more complete and closer to the actual engineering situation.

The remainder of this article is structured as follows. Section II introduces the general transient output characteristics of REG systems considering their typical sequential switching schemes. Section III establishes the equivalent rotor swing equations of REG systems for different fault stages. Section IV analyses the transient synchronization characteristics of REG systems based on the proposed equivalent rotor swing equations. In Section V, the transient synchronization stability criterion is deduced and the possible instability phenomenon in the entire grid fault process is explained. Section VI validates the analytical results of simulation and experimental results. Finally, Section VII concludes this article.

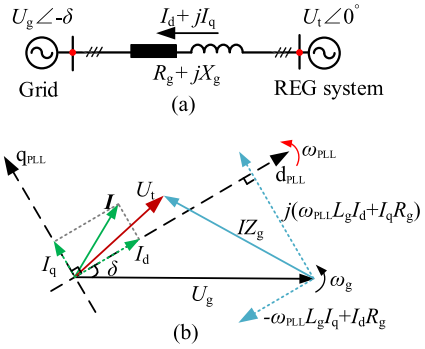

Fig. 1. (a) Simplified schematic of REG system. (b) Voltage vector diagram of the grid-connected REG system in the *d/q*-axis rotating frame.

II. Output Characteristics of Grid-Connected REG Systems Considering PLL Nonlinear Behaviors

Typical control structures for a PLL-based grid-connected REGs system such as DFIG and VSC systems have been widely investigated in previous studies [17]–[20], in which the PLL controller was adopted to synchronize with the power grid. On this basis, the general simplified schematic of the REG system is shown in Fig. 1(a), and the voltage vector diagram of output characteristics of the grid-connected REG system in the d/q-axis rotating frame is shown in Fig. 1(b).

The REG terminal voltage in the *d/q*-axis rotating frame can be expressed as

$$\begin{cases} U_{\mathrm{td}} = U_{\mathrm{g}}\cos\delta + R_{\mathrm{g}}I_{\mathrm{d}} - \omega_{\mathrm{PLL}}L_{\mathrm{g}}I_{\mathrm{q}} \\ U_{\mathrm{tq}} = -U_{\mathrm{g}}\sin\delta + R_{\mathrm{g}}I_{\mathrm{q}} + \omega_{\mathrm{PLL}}L_{\mathrm{g}}I_{\mathrm{d}} \end{cases} \tag{1}$$

where δ is the phase difference between the *d*-axis reference frame of the PLL and the grid voltage vector U_{g}.

From Fig. 1(b), it is clear that the PLL is employed to align the *d*-axis in the PLL-synchronized two-phase rotating reference frame with the terminal voltage, which is the only loop to maintain the grid-connected REG system synchronously running with the power grid. In addition, it is generally accepted that the *d*-axis and *q*-axis current instructions represent active and reactive power instructions, respectively, which is expressed as

$$\begin{cases} P^* = U_{\mathrm{td}}I_{\mathrm{d}}^* \\ Q^* = -U_{\mathrm{td}}I_{\mathrm{q}}^*. \end{cases} \tag{2}$$

Moreover, Fig. 1 also shows that δ could present the synchronization state for the REG system. Correspondingly, δ can be defined as the EPA, and the variation in EPA caused by the imbalanced angular frequency between PLL and $\boldsymbol{U_{\mathrm{g}}}$ can be expressed as

$$\frac{d\delta}{dt} = \omega_{\mathrm{b}}(\omega_{\mathrm{PLL}} - \omega_{\mathrm{g}}). \tag{3}$$

Considering that different types of PLL controllers have the same phase locking principle as the typical PLL controller [16], the controller structure of the typical PLL can be regarded as a study example; it is shown in Fig. 2.

Fig. 2 shows that the *q*-axis component of $\boldsymbol{U_{\mathrm{t}}}$ is regulated by a proportional integral (PI) controller for phase tracking to

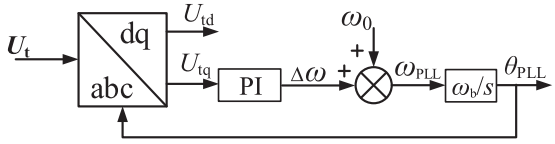

Fig. 2. Typical PLL controller structure.

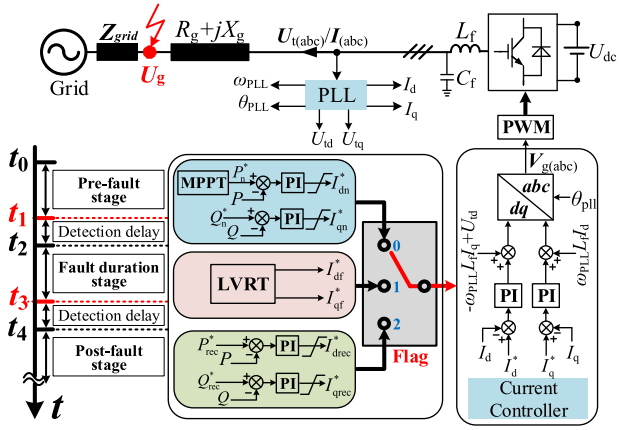

Fig. 3. Typical configuration diagram and sequential switching control for VSC system when facing a grid fault.

achieve the terminal voltage vector orientation. Therefore, the PLL model is described as (4). Furthermore, the change rate of ω_{PLL} is expressed as (5) follows:

$$\omega_{\mathrm{PLL}} = k_{\mathrm{pp}}U_{\mathrm{tq}} + k_{\mathrm{ip}}\int U_{\mathrm{tq}}dt + \omega_0 \tag{4}$$

$$\frac{d\omega_{\mathrm{PLL}}}{dt} = k_{\mathrm{pp}}\frac{dU_{\mathrm{tq}}}{dt} + k_{\mathrm{ip}}U_{\mathrm{tq}}. \tag{5}$$

From (3)–(5), it can be derived that U_{tq} will cause a variation of ω_{PLL}, and then drive $\boldsymbol{U_{\mathrm{t}}}$ to keep the synchronization with $\boldsymbol{U_{\mathrm{g}}}$ by eliminating U_{tq} to zero to enable the REG to synchronously run with the power grid.

However, these REG systems have different control objectives under different grid conditions, which lead to a sequential switch of control strategies in response to the variations in grid conditions during the entire grid fault process. The VSC is s a commonly used topological structure in typical REG systems, this makes it suitable as a study case [27].

In Fig. 3, t_1 and t_3 are fault time and fault clearing time, respectively.

Fig. 3 shows the sequential switching control of the VSC system for the entire grid fault process. The transient responses can be divided into 5 stages, which are discussed as follows.

1) *Prefault stage ($t_0 \rightarrow t_1$):* The grid fault has not occurred (Flag = 0), the VSC system operates at maximum power point tracking (MPPT) mode and is in a steady state, which means $P = P_{\mathrm{n}}^*$ and $Q = Q_{\mathrm{n}}^*$.
2) *Fault dead-time stage ($t_1 \rightarrow t_2$):* The grid fault occurs at time t_1; however, the LVRT control strategy has not been switched in because of the detection delay. Flag = 0 still holds.

3) *Fault duration stage ($t_2 \rightarrow t_3$):* The grid fault is detected at time t_2 and the LVRT strategy is simultaneously triggered (Flag = 1).
4) *Fault recovery dead-time stage ($t_3 \rightarrow t_4$):* The grid fault is cleared at time t_3, but the LVRT control strategy has not been interrupted because of the detection delay. Flag = 1 still holds.
5) *Postfault stage ($t_4 \rightarrow \infty$):* The cleared grid fault is detected at time, t_4 and the VSC system is restored to the unit power factor operation mode. The output active power is also restored to the normal value at the required rate according to grid codes (Flag = 2). It is noted that, although the VSC system re-enter the constant power control mode during the postfault stage, but its active power instruction needs to restore to the normal value at the required rate according to grid codes, rather than adopting MPPT control mode directly. So that the power loop structure during postfault stage is inconsistent slightly with that of prefault stage.

Generally, the grid side L of the *LCL*-type filter is much smaller than that of equivalent inductance existed in the transmission lines and transformers, which can be converted to a part of the equivalent grid impedance. With the impedance conversion, no matter whether *LCL*-type filter or *LC*-type filter is used in the grid-connected VSC system, the corresponding equivalent mathematical model can be established in a unified form of the grid-connected VSC system with an *LC*-type filter after the impedance conversion in PLL timescale. In addition, the bandwidth of the VSC current control loop is considerably larger than that of PLL. That is, the current regulation of the VSC is quick in contrast to the dynamics of PLL, thus the REG system can be regarded as a controlled current source in PLL reference frame [17]–[20]. As a result, when the transient synchronization stability issue is studied in PLL timescale, the regulation of the alternating current (ac) control can be reasonably neglected, which means $\boldsymbol{I} = \boldsymbol{I}^*$, shown as

$$\begin{cases} I_{\mathrm{d}} = I_{\mathrm{d}}^* \\ I_{\mathrm{q}} = I_{\mathrm{q}}^*. \end{cases} \tag{6}$$

III. Equivalent Rotor Swing Equation for Grid-Connected REG System During Different Fault Stages

A. Synchronization Model During Prefault Stage

As seen in Fig. 3, the aim of the VSC system is to achieve MPPT and to control the output reactive power under normal grid conditions. Correspondingly, both the outer power control loop and inner current controller are adopted during the prefault stage. In addition, Tang *et al.* [18] indicated that the active/reactive power control loops belong to electromechanical timescale (rotor speed control timescale), such that the *d*/*q*-axis current instructions can be approximately obtained through the algebraic equation of the active/reactive power instruction during the prefault stage, which is given as follows:

$$\begin{cases} I_{\mathrm{d}}^* = \frac{P_{\mathrm{n}}^*}{U_{\mathrm{tdn}}} \\ I_{\mathrm{q}}^* = \frac{Q_{\mathrm{n}}^*}{-U_{\mathrm{tdn}}}. \end{cases} \tag{7}$$

Substituting (6) and (7) into (1), the *dq*-axis components of $\boldsymbol{U_{\mathrm{t}}}$ can be expressed as (8) during the prefault stage

$$\begin{cases} U_{\mathrm{tdn}} = U_{\mathrm{gn}} \cos\delta + R_{\mathrm{g}} \frac{P_{\mathrm{n}}^*}{U_{\mathrm{tdn}}} + \omega_{\mathrm{PLL}} L_{\mathrm{g}} \frac{Q_{\mathrm{n}}^*}{U_{\mathrm{tdn}}} \\ U_{\mathrm{tqn}} = -U_{\mathrm{gn}} \sin\delta - R_{\mathrm{g}} \frac{Q_{\mathrm{n}}^*}{U_{\mathrm{tdn}}} + \omega_{\mathrm{PLL}} L_{\mathrm{g}} \frac{P_{\mathrm{n}}^*}{U_{\mathrm{tdn}}} \end{cases} \tag{8}$$

where Q_{n}^* is generally set to zero to realize unit power factor operation, such that I_{q}^* is also approximately equal to zero during the prefault stage. Moreover, the change rate of U_{tdn} and U_{tqn} can be deduced as

$$\begin{cases} \frac{dU_{\mathrm{tdn}}}{dt} = -U_{\mathrm{gn}} s\mathrm{in}\delta \frac{d\delta}{dt} - \frac{R_{\mathrm{g}} P_{\mathrm{n}}^*}{U_{\mathrm{tdn}}^2} \frac{dU_{\mathrm{tdn}}}{dt} + \frac{L_{\mathrm{g}} Q_{\mathrm{n}}^*}{U_{\mathrm{tdn}}} \frac{d\omega_{\mathrm{PLL}}}{dt} \\ \qquad - \frac{\omega_{\mathrm{PLL}} L_g Q_{\mathrm{n}}^*}{U_{\mathrm{tdn}}^2} \frac{dU_{\mathrm{tdn}}}{dt} \\ \frac{dU_{\mathrm{tqn}}}{dt} = -U_{\mathrm{gn}} \cos\delta \frac{d\delta}{dt} + \frac{R_{\mathrm{g}} Q_{\mathrm{n}}^*}{U_{\mathrm{tdn}}^2} \frac{dU_{\mathrm{tdn}}}{dt} + \frac{L_{\mathrm{g}} P_{\mathrm{n}}^*}{U_{\mathrm{tdn}}} \frac{d\omega_{\mathrm{PLL}}}{dt} \\ \qquad - \frac{\omega_{\mathrm{PLL}} L_g P_{\mathrm{n}}^*}{U_{\mathrm{tdn}}^2} \frac{dU_{\mathrm{tdn}}}{dt}. \end{cases} \tag{9}$$

It can be seen from (9) that the change rate of U_{tqn} is related with U_{tdn} and its change rate. Consequently, the analytic expression of U_{tdn} and its change rate can be deduced as the following mathematical form of (10) by substituting, respectively, $Q_{\mathrm{n}}^* = 0$ into (8) and substituting (3) into (9)

$$\begin{cases} U_{\mathrm{tdn}} = \frac{U_{\mathrm{gn}} \cos\delta + \sqrt{(U_{\mathrm{gn}} \cos\delta)^2 + 4 R_{\mathrm{g}} P_{\mathrm{n}}^*}}{2} \\ \frac{dU_{\mathrm{tdn}}}{dt} = -\frac{U_{\mathrm{tdn}}^2 U_{\mathrm{gn}} \omega_{\mathrm{b}} \sin\delta}{U_{\mathrm{tdn}}^2 + R_{\mathrm{g}} P^*} (\omega_{\mathrm{PLL}} - \omega_{\mathrm{g}}). \end{cases} \tag{10}$$

Equation (10) shows that the value of U_{tdn} is a function of δ when U_{gn}, P_{n}^*, and R_g are given. Similarly, the change rate of U_{tqn} is obtained as (11) by substituting (10) into (9)

$$\frac{dU_{\mathrm{tqn}}}{dt} = U_{\mathrm{gn}} \omega_{\mathrm{b}} \left(\frac{\omega_{\mathrm{PLL}} L_g P_{\mathrm{n}}^*}{U_{\mathrm{tdn}}^2 + R_{\mathrm{g}} P_{\mathrm{n}}^*} s\mathrm{in}\delta - \cos\delta \right) (\omega_{\mathrm{PLL}} - \omega_{\mathrm{g}}) + \frac{L_{\mathrm{g}} P_{\mathrm{n}}^*}{U_{\mathrm{td}}} \frac{d\omega_{\mathrm{PLL}}}{dt}. \tag{11}$$

As previously mentioned, U_{tqn} causes a variation in ω_{PLL}, such that the characteristics of the grid-connected VSC system can be further deduced as (12) by substituting (11) into (5)

$$\underbrace{\frac{1}{k_{\mathrm{ip}}} \left(1 - \frac{k_{pp} L_{\mathrm{g}} P_{\mathrm{n}}^*}{U_{\mathrm{tdn}}} \right)}_{J_{v0}} \frac{d\omega_{\mathrm{PLL}}}{dt} = \underbrace{0 - \left(U_{\mathrm{gn}} s\mathrm{in}\delta - \frac{\omega_{\mathrm{g}} L_{\mathrm{g}} P_{\mathrm{n}}^*}{U_{\mathrm{tdn}}} \right)}_{T_{\mathrm{v0}}^* - T_{v0}}$$

$$\underbrace{- \left[\frac{k_{pp} U_{\mathrm{gn}} \omega_{\mathrm{b}}}{k_{\mathrm{ip}}} \left(\cos\delta - \frac{\omega_{\mathrm{PLL}} L_{\mathrm{g}} P_{\mathrm{n}}^*}{U_{\mathrm{tdn}}^2 + R_{\mathrm{g}} P_{\mathrm{n}}^*} \sin\delta \right) - \frac{L_{\mathrm{g}} P_{\mathrm{n}}^*}{U_{\mathrm{tdn}}} \right]}_{D_{v0}} (\omega_{\mathrm{PLL}} - \omega_{\mathrm{g}}). \tag{12}$$

Combining (10) and (12), both J_{v0} and D_{v0} become functions of δ. From (12), the synchronization behaviors of VSC are determined by the virtual torque difference and damping term. As a result, (12) becomes the VSC's equivalent rotor swing equation during the prefault stage, which has the similar form as that of SGs, and can present the synchronization characteristics of grid-connected VSC systems during the prefault stage.

B. Transient Synchronization Model During Fault Dead-Time Stage

Once a grid fault occurs, the present mainstream voltage detection methods produce a detection delay from 5 ms up

to 20 ms [30], [31]. That is, the VSC system enters the fault dead-time stage before the grid drop is detected. Thus, both the control mode and power instructions are consistent with those of the prefault stage, although the voltage drop has occurred.

When grid voltage drops from $U_{\rm gn}$ to $U_{\rm gf}$, $U_{\rm td}$ decreases from $U_{\rm tdn}$ to $U_{\rm tdf}$ as well. $U_{\rm tdf}$ can be also calculated referring to (10). The voltage sag will further lead to an increase for the *d*-axis current instruction shown as follows:

$$I_{\rm d}^{*}=\begin{cases}\frac{P_{\rm n}^{*}}{U_{\rm tdf}},(\frac{P_{\rm n}^{*}}{U_{\rm tdf}}<I_{\rm dm})\\ I_{\rm dm}\ ,(\frac{P_{\rm n}^{*}}{U_{\rm tdf}}\geq I_{\rm dm}).\end{cases}\tag{13}$$

Equation (13) shows that the VSC system may turn into a saturated current source if the active power instruction is over large or the voltage drop is over deep. Once VSC system turns into the saturated current source, the expressions of $U_{\rm tdf}$ and $U_{\rm tqf}$ become (14), which is obtained by substituting (12) and $Q_{\rm n}^{*}=0$ into (8)

$$\begin{cases}U_{\rm tdf}=U_{\rm gf}\cos\delta+R_{\rm g}I_{\rm dm}\\ U_{\rm tqf}=-U_{\rm gf}\sin\delta+\omega_{\rm PLL}L_{\rm g}I_{\rm dm}.\end{cases}\tag{14}$$

It can be seen from (14) that the dynamics of the *d*-axis current are eliminated as it is limited to a fixed value during fault dead-time stage. Correspondingly, the change rate of $U_{\rm tdf}$ and $U_{\rm tqf}$ will be expressed as

$$\begin{cases}\frac{dU_{\rm tdf}}{dt}=-U_{\rm gf}sin\delta\frac{d\delta}{dt}\\ \frac{dU_{\rm tqf}}{dt}=-U_{\rm gf}\cos\delta\frac{d\delta}{dt}+L_{\rm g}I_{\rm dm}\frac{d\omega_{\rm PLL}}{dt}.\end{cases}\tag{15}$$

Substituting (15) and (3) into (5), transient characteristics of the grid-connected VSC system are expressed as

$$\underbrace{\left(\frac{1-k_{\rm pp}L_{\rm g}I_{\rm dm}}{k_{\rm ip}}\right)}_{J_{v1}}\frac{d\omega_{\rm PLL}}{dt}=\underbrace{0-(U_{\rm gf}sin\delta-\omega_{\rm g}L_{\rm g}I_{\rm dm})}_{T_{\rm v1}^{*}-T_{v1}}-\underbrace{\left[\frac{k_{\rm pp}U_{\rm gf}\omega_{\rm b}}{k_{\rm ip}}\cos\delta-L_{\rm g}I_{\rm dm}\right]}_{D_{v1}}(\omega_{\rm PLL}-\omega_{\rm g})\tag{16}$$

where $J_{\rm v1}$ is a certain value, and $D_{\rm v1}$ is a function of δ.

Similar to (12), (16) is also named as the VSC's equivalent rotor swing equation during fault dead-time stage. If the VSC system does not turn into a saturated current source, its transient synchronization characteristics during fault dead-time stage are similar to those of the prefault stage, which could also be described by (12), only replacing $U_{\rm gn}$ by $U_{\rm gf}$.

C. Transient Synchronization Model During Fault Duration Stage

When the grid voltage drop is detected, the LVRT control strategy is immediately adopted, which is illustrated in Fig. 3. To realize a fast active/reactive current injection during LVRT, the VSC system directly adopts constant current control mode. It is also generally accepted by the industrial circles and academia, and has been widely used in the commercial renewable power generation [13], [28], [29]. As a result, the *d/q*-axis current instruction is set as

$$\begin{cases}I_{\rm d}^{*}=I_{\rm df}^{*}\\ I_{\rm q}^{*}=I_{\rm qf}^{*}.\end{cases}\tag{17}$$

Therefore, the expressions of $U_{\rm tdf}$ and $U_{\rm tqf}$ become (18) during LVRT, which is obtained by substituting (17) into (1)

$$\begin{cases}U_{\rm tdf}=U_{\rm gf}\cos\delta+R_{\rm g}I_{\rm df}^{*}-\omega_{\rm PLL}L_{\rm g}I_{\rm qf}^{*}\\ U_{\rm tqf}=-U_{\rm gf}\sin\delta+R_{\rm g}I_{\rm qf}^{*}+\omega_{\rm PLL}L_{\rm g}I_{\rm df}^{*}.\end{cases}\tag{18}$$

Equation (18) shows that the dynamics of the *d/q*-axis currents are eliminated as they are set as certain values during LVRT. Correspondingly, the change rates of $U_{\rm tdf}$ and $U_{\rm tqf}$ are given as

$$\begin{cases}\frac{dU_{\rm tdf}}{dt}=-U_{\rm gf}sin\delta\frac{d\delta}{dt}-L_{\rm g}I_{\rm qf}^{*}\frac{d\omega_{\rm PLL}}{dt}\\ \frac{dU_{\rm tqf}}{dt}=-U_{\rm gf}\cos\delta\frac{d\delta}{dt}+L_{\rm g}I_{\rm df}^{*}\frac{d\omega_{\rm PLL}}{dt}.\end{cases}\tag{19}$$

Substituting (19) and (3) into (5), the VSC's equivalent rotor swing equation during LVRT is expressed as

$$\underbrace{\left(\frac{1-k_{\rm pp}L_{\rm g}I_{\rm df}^{*}}{k_{\rm ip}}\right)}_{J_{v2}}\frac{d\omega_{\rm PLL}}{dt}=\underbrace{0-(U_{\rm gf}sin\delta-\omega_{\rm g}L_{\rm g}I_{\rm df}^{*}-R_{\rm g}I_{\rm qf}^{*})}_{T_{\rm v2}^{*}-T_{v2}}-\underbrace{\left[\frac{k_{\rm pp}U_{\rm gf}\omega_{\rm b}}{k_{\rm ip}}\cos\delta-L_{\rm g}I_{\rm df}^{*}\right]}_{D_{v2}}(\omega_{\rm PLL}-\omega_{\rm g}).\tag{20}$$

D. Transient Synchronization Model During Fault Recovery Dead-Time Stage

The grid voltage is restored to the normal level $U_{\rm gn}$ when the grid fault is cleared. However, the *d/q*-axis current instructions remain the same as those of the fault duration stage because of the detection delay, which is shown as (17). Consequently, VSC's equivalent swing equation during fault recovery dead-time stage could also be approximatively expressed by (20), only replacing $U_{\rm gf}$ by $U_{\rm gn}$.

E. Synchronization Model During Postfault Stage

When the restored grid voltage is detected by the VSC system, the unit power factor operation mode is triggered again, as shown in Fig. 3. Consequently, the active/reactive power instruction are set to $P_{\rm rec}^{*}$ and 0, respectively, which is similar to the prefault stage. Correspondingly, the equivalent swing equation during postfault stage could also be expressed by (12), only replacing $P_{\rm n}^{*}$ by $P_{\rm rec}^{*}$.

IV. Synchronization Characteristic Analysis for Grid-Connected REG System

According to the proposed synchronization models in Section III, the synchronization characteristics of the VSC system during different fault stages can be presented by the form of equivalent rotor swing equations with different parameters, which can be summarized as (21) and Table I

$$J_{{\rm v}x}\frac{d\omega_{\rm PLL}}{dt}=T_{{\rm v}x}^{*}-T_{vx}-D_{{\rm v}x}(\omega_{\rm PLL}-\omega_{\rm g})\tag{21}$$

where *x* represents the number of each grid fault stage.

The relationship among the grid status, control mode, and deduced synchronous characteristic indexes is displayed in Table I. It can be concluded that $J_{{\rm v}x}$ can reflect the sensitivity of the change of $\omega_{\rm PLL}$. The expressions of $J_{{\rm v}x}$ among different fault stages show that a smaller $k_{\rm ip}$ is beneficial to the virtual inertia

TABLE I
PARAMETERS OF THE EQUIVALENT ROTOR SWING EQUATIONS OF THE VSC SYSTEM AT DIFFERENT FAULT STAGES

x	Grid fault stage	Grid voltage (U_g)	Control mode	Virtual prime mover torque T_{vx}^*	Virtual output torque T_{vx}	Virtual inertia (J_{vx})	Virtual damping coefficient (D_{vx})
0	Prefault stage	U_{gn}	Power source	0	$U_{gn}\sin\delta - \frac{\omega_g L_g P_n^*}{U_{tdn}}$	$\frac{1}{k_{ip}}(1-\frac{k_{pp}L_g P_n^*}{U_{tdn}})$	$\frac{k_{pp}U_{gn}\omega_b}{k_{ip}}(\cos\delta - \frac{\omega_{PLL}L_g P_n^*}{U_{tdn}^2+R_g P_n^*}\sin\delta) - \frac{L_g P_n^*}{U_{tdn}}$
1	Fault dead-time stage	U_{gf}	Power source	0	$U_{gf}\sin\delta - \frac{\omega_g L_g P_n^*}{U_{tdf}}$	$\frac{1}{k_{ip}}(1-\frac{k_{pp}L_g P_n^*}{U_{tdf}})$	$\frac{k_{pp}U_{gf}\omega_b}{k_{ip}}(\cos\delta - \frac{\omega_{PLL}L_g P_n^*}{U_{tdf}^2+R_g P_n^*}\sin\delta) - \frac{L_g P_n^*}{U_{tdf}}$
			Saturated current source	0	$U_{gf}\sin\delta - \omega_g L_g I_{dm}$	$\frac{1-k_{pp}L_g I_{dm}}{k_{ip}}$	$\frac{k_{pp}U_{gf}\omega_b}{k_{ip}}\cos\delta - L_g I_{dm}$
2	Fault duration stage	U_{gf}	Current source	0	$U_{gf}\sin\delta - \omega_g L_g I_{df}^* - R_g I_{qf}^*$	$\frac{1-k_{pp}L_g I_{df}^*}{k_{ip}}$	$\frac{k_{pp}U_{gf}\omega_b}{k_{ip}}\cos\delta - L_g I_{df}^*$
3	Fault recovery dead-time stage	U_{gn}	Current source	0	$U_{gn}\sin\delta - \omega_g L_g I_{df}^* - R_g I_{qf}^*$	$\frac{1-k_{pp}L_g I_{df}^*}{k_{ip}}$	$\frac{k_{pp}U_{gn}\omega_b}{k_{ip}}\cos\delta - L_g I_{df}^*$
4	Posfault stage	U_{gn}	Power source	0	$U_{gn}\sin\delta - \frac{\omega_g L_g P_{rec}^*}{U_{tdn}}$	$\frac{1}{k_{ip}}(1-\frac{k_{pp}L_g P_{rec}^*}{U_{tdn}})$	$\frac{k_{pp}U_{gn}\omega_b}{k_{ip}}(\cos\delta - \frac{\omega_{PLL}L_g P_{rec}^*}{U_{tdn}^2+R_g P_{rec}^*}\sin\delta) - \frac{L_g P_{rec}^*}{U_{tdn}}$

of the VSC system. However, the higher the k_{pp}, the higher the L_g, and more active power or d-axis current injection would decrease the value of J_{vx}.

The virtual damping coefficient (D_{vx}) shows the VSC system ability to suppress the deviation of ω_{PLL}. A smaller k_{ip}, higher k_{pp}, and higher U_g would increase the value of D_{vx} among different fault stages, which could enhance the synchronization stability of the VSC system. The D_{vx} can be significantly improved when $\delta = 0$ in each fault stage. These findings are in agreement with results from the literature [20]–[22]. In addition, D_{vx} significantly changes with δ, which is not a constant value. Therefore, it is necessary to keep D_{vx} positive, otherwise the control system of VSC would become a positive feedback system, and the LOS phenomenon may occur.

Consequently, both the J_{vx} and D_{vx} of the VSC system must remain positive.

A. Characteristics Analysis of Synchronous Characteristic Indexes Among Different Fault Stages

The switching of system operation states among different fault stages changes J_{vx} and D_{vx}, which is discussed as follows.

1) During the prefault stage, the grid voltage U_g is maintained to the normal level U_{gn}, such that J_{v0} and D_{v0} are high values.
2) When the VSC system enters the fault dead-time stage, the grid voltage drops to U_{gf}, but the active power instruction is not yet adjusted. By comparing J_{v0} and J_{v1} as well as D_{v0} and D_{v1}, it is clear that the deeper the grid voltage drop, the smaller the virtual inertia and virtual damping coefficient of the system.
3) The LVRT control strategy is adopted when the VSC system enters the fault duration stage. As a result, the reduced d-axis current instruction can increase VSC's virtual inertia to J_{v2}. In addition, appropriate d/q-axis current instructions may adjust the value of δ, which can also increase VSC's virtual damping coefficient to D_{v2}, thus enhancing the synchronization stability of the VSC system.
4) When the VSC system enters the fault recovery dead-time stage, it is shown in Table I that the grid state cannot affect the VSC virtual inertia under current source mode, although the grid voltage is restored to U_{gn}, and J_{v3} becomes equal to J_{v2}. However, the restored grid voltage can considerably improve the virtual damping coefficient, such that the Dv3 becomes higher than Dv2.
5) When postfault stage initiates, the VSC system reverts to power control mode, which has a similar virtual inertia and virtual damping coefficient characteristics as the prefault stage. However, the active power instruction P_{rec}^* is considerably lower than P_n^* according to grid codes. As a result, both the J_{v4} and D_{v4} values are restored to a high level.

B. Relationship Analysis Between the Imbalanced Virtual Torque and the Angular Frequency/Magnitude States of Terminal Voltage

The synchronization properties of the VSC system are caused by the virtual torque difference. $(T_{vx}^* - T_{vx})>0$ will lead to an increase in ω_{PLL}, which will regulate δ to increase and further increase T_{vx} to balance with T_{vx}^*. Similarly, $(T_{vx}^* - T_{vx})<0$ will result in a decrease in ω_{PLL}, which will reduce δ, thus, the T_{vx} will also be decreased to eliminate the virtual torque difference.

Table I shows that T_{vx}^* is always zero and unaffected by different operation conditions. However, either the switching of control modes or the change of grid voltage state would cause a deviation of T_{vx}, thus driving the motions of ω_{PLL} and δ. T_{vx} is essentially a steady-state value of $-U_{tq}$. The diagram of the VSC equivalent rotor swing equation is shown in Fig. 4.

Therefore, the physical meaning of (21) and Fig. 4 can be explained as follows: the deviation in ω_{PLL} is essentially driven by

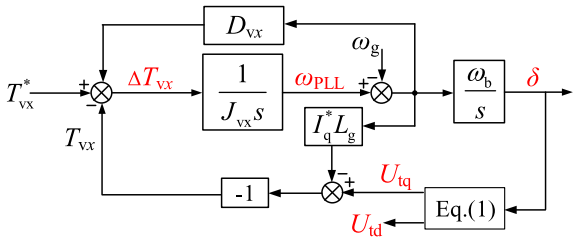

Fig. 4. Diagram of VSC's equivalent rotor swing equation.

the imbalanced q-axis voltage component of $\boldsymbol{U_t}$. The deviation in ω_{PLL} causes a motion of δ. As δ changes, T_{vx} is gradually regulated towards 0, which is aimed to counteract U_{tq}. However, it can be seen from (1) and Fig. 4 that the deviation in ω_{PLL} and δ affects the values of U_{tq} and U_{td}. This implies that both the angular frequency/magnitude states of $\boldsymbol{U_t}$ are simultaneously changing.

Furthermore, the actual output active/reactive powers are expressed as

$$\begin{cases} P = U_{\mathrm{td}} I_{\mathrm{d}}^* + U_{\mathrm{tq}} I_{\mathrm{q}}^* \\ Q = -U_{\mathrm{td}} I_{\mathrm{q}}^* + U_{\mathrm{tq}} I_{\mathrm{d}}^*. \end{cases} \tag{22}$$

As shown in a comparison with (2), the imbalanced q-axis voltage would further cause the imbalanced active/reactive powers, which is shown as

$$\begin{cases} \Delta P = P^* - P = -U_{\mathrm{tq}} I_{\mathrm{q}}^* \\ \Delta Q = Q^* - Q = -U_{\mathrm{tq}} I_{\mathrm{d}}^*. \end{cases} \tag{23}$$

In (22) and (23), U_{tq} interacts with I_{q} to produce imbalanced active power, such that (21) can be transformed to (24) by multiplying both sides of (21) by $-I_{\mathrm{q}}^*$

$$(-I_{\mathrm{q}}^*) J_{vx} \frac{d\omega_{\mathrm{PLL}}}{dt} = P_x^* - P_x - (-I_{\mathrm{q}}^*) D_{vx} (\omega_{\mathrm{PLL}} - \omega_{\mathrm{g}}). \tag{24}$$

As can be seen from (24), the excess/shortage active power accelerates/decelerates ω_{PLL} until P equals P^*. In addition, from a mathematical perspective, the value of q-axis current affects the expressions of J_{vx} and D_{vx}.

Similarly, (21) can be transformed to (25) by multiplying both sides of (21) by $-I_{\mathrm{d}}^*$, which means that the interaction between U_{tq} and the d-axis current produces imbalanced reactive power

$$(I_{\mathrm{d}}^* J_{vx}) \frac{d\omega_{\mathrm{PLL}}}{dt} = -(Q_x^* - Q_x) - (I_{\mathrm{d}}^* D_{vx})(\omega_{\mathrm{PLL}} - \omega_{\mathrm{g}}). \tag{25}$$

It is shown in (25) that the shortage/excess reactive power accelerates/decelerates the ω_{PLL} until Q equals Q^*. In addition, the value of the d-axis current affects the expressions of virtual inertia and virtual damping coefficient.

Equations (24) and (25) show that both the imbalanced active and reactive powers could result in a deviation in ω_{PLL}, which would further cause a motion of δ. It should be emphasized that the imbalanced reactive/active power is produced by the interaction between U_{tq} and d/q-axis current components, which is essentially caused because the PLL cannot eliminate U_{tq} to zero.

Consequently, the imbalanced q-axis component of $\boldsymbol{U_t}$ is the fundamental cause of the virtual imbalanced torque, which drives a motion of ω_{PLL} and EPA. The affected ω_{PLL} and δ in turn affect the amplitude of the terminal voltage. Therefore, the VSC system presents synchronization behavior of voltage-frequency coupling characteristics. In addition, the VSC system can interact with the grid based on its virtual inertia and virtual damping term, but the synchronization property of the VSC system is determined by its control structure rather than its inherent kinematic property, as occurs for SGs. Moreover, the improper control parameters or nonideal operating state may also cause synchronization instability issues for the VSC system, and the corresponding criteria are further studied in Section V.

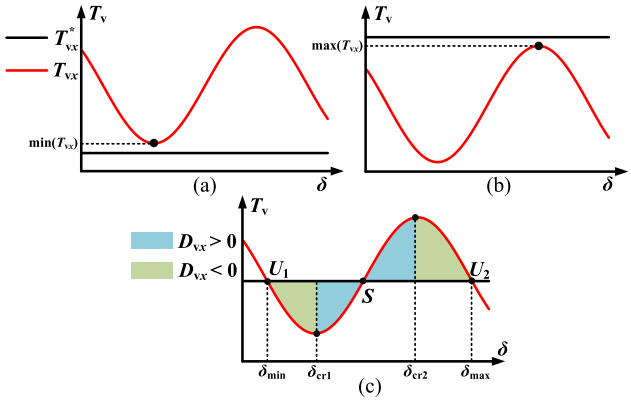

Fig. 5. Relationship between T^*_{vx} and T_{vx}. (a) Minimum value of $T_{\mathrm{v}x}$ is higher than that of T^*_{vx}. (b) Maximum value of $T_{\mathrm{v}x}$ is lower than that of T^*_{vx}. (c) Stable and unstable equilibrium points.

V. Stability Criteria for the Grid-Connected REG System

According to Section III, the synchronization characteristics of the grid-connected VSC system can be represented as the mathematical form of equivalent rotor swing equations, which have a form identical to those for traditional SGs. Consequently, the stability criterion of the VSC system can also refer to that of SGs.

A. Criterion I: Existence of Equilibrium Points

According to (21), the imbalanced virtual torque between T^*_{vx} and $T_{\mathrm{v}x}$ will accelerate or decelerate ω_{PLL} until $T_{\mathrm{v}x}$ equals T^*_{vx}, which implies that the VSC system does not have an equilibrium point if $T_{\mathrm{v}x}$ does not equal T^*_{vx}. There are two different cases discussed as follows.

1) When the minimum value of T_{vx} is larger than T^*_{vx}, which is shown in Fig. 5(a), there is no intersection between the curves of T_{vx} and T^*_{vx}; thus, ωPLL continues decreasing and the LOS phenomenon for angular frequency reduction occurs.
2) When the maximum value of T_{vx} is lower than T^*_{vx}, as shown in Fig. 5(b), the excess of T_{*vx} always exists because $T^*_{\mathrm{vx}} > T_{\mathrm{vx}}$. Thus, ωPLL continues increasing and the LOS phenomenon for angular frequency increase occurs.
3) In addition, D_{vx} must be positive for the VSC system to stably operate at an equilibrium point. Consequently, the EPA of the VSC system must run within $[\delta_{\mathrm{cr1}}, \delta_{\mathrm{cr2}}]$

during static or quasi-static stages, shown in Fig. 5(c) according to the expressions of Dvx. Thus, point S is the only stable equilibrium point of the VSC system, whereas points U1 and U2 are unstable points. $\delta_{\rm cr1}$ and $\delta_{\rm cr2}$ are the static or quasi-static stability limits of the VSC system, respectively. Thus, the VSC system cannot maintain a long-term stable operation when EPA exceeds $[\delta_{\rm cr1}, \delta_{\rm cr2}]$ during static or quasi-static stages, but EPA can briefly exceed $[\delta_{\rm cr1}, \delta_{\rm cr2}]$ during the transient/dynamic regulation processes. However, $\delta_{\max}$ and $\delta_{\min}$ are the transient synchronization stability limits of the VSC system during the transient synchronization process. Thus, the EPA of the VSC system cannot exceed $[\delta_{\max1}, \delta_{\max2}]$ in either steady state or transient/dynamic regulation process.

Consequently, the VSC system must meet criterion (26) to ensure that the system has an equilibrium point at each fault stage

$$[\max(T_{vx}) \geq T_{\rm vx}^*] \cap [\min(T_{vx}) \leq T_{\rm vx}^*] \cap [\delta \in (\delta_{\rm cr1}, \delta_{\rm cr2})]. \tag{26}$$

B. Criterion II: Equal Area Criterion

Criterion I can only evaluate the existence of the equilibrium point. However, the transient synchronization behaviors may result in a failure of the VSC system to reach the desired equilibrium point during the transient synchronization process. Thus, LOS is possible even if the VSC system meets *Criterion I*.

The EAC is a typical method for assessing the transient stability of SG based on its rotor swing equation. This method can be equivalently applied to the VSC system according to the proposed equivalent rotor swing equation shown in Table I. The derivation steps of the EAC for VSC systems are as follows. According to (3), the change rate of $\omega_{\rm PLL}$ can be expressed as

$$\frac{d\omega_{\rm PLL}}{dt} = \frac{1}{\omega_{\rm b}} \cdot \frac{d^2\delta}{dt^2} = \frac{1}{\omega_{\rm b}} \cdot \frac{d}{dt}\left(\frac{d\delta}{dt}\right) = \frac{1}{\omega_{\rm b}} \cdot \ddot{\delta} = \frac{1}{\omega_{\rm b}} \dot{\delta} \cdot \frac{d\dot{\delta}}{d\delta}. \tag{27}$$

Integrating both sides of (27) with respect to t, we obtain

$$\frac{J_{\rm vx}}{\omega_{\rm b}} \int \ddot{\delta} \cdot dt = \int (T_{\rm vx}^* - T_{vx}) \cdot dt - \int D_{\rm vx}(\omega_{\rm PLL} - \omega_{\rm g}) \cdot dt. \tag{28}$$

Multiplying both sides of (28) by $\dot{\delta}$, (27) is expressed as

$$\begin{cases} d\delta = \dot{\delta} \cdot dt \\ \frac{J_{\rm vx}}{\omega_{\rm b}} \int \ddot{\delta} \cdot d\delta = \int (T_{\rm vx}^* - T_{vx}) \cdot d\delta - \int D_{\rm vx}(\omega_{\rm PLL} - \omega_{\rm g}) \cdot d\delta. \end{cases} \tag{29}$$

The calculation result is derived as

$$\underbrace{\int_{\delta_0}^{\delta_{\rm t}} (T_{\rm vx}^* - T_{vx}) d\delta}_{\text{virtual potentialenergy}} = \underbrace{\frac{1}{2}\omega_{\rm b} J_{vx}(\omega_{\rm PLL} - \omega_{\rm g})^2 \Big|_{\delta_0}^{\delta_{\rm t}}}_{\text{virtual kineticenergy}} + \underbrace{\frac{1}{\omega_{\rm b}} \int_{\delta_0}^{\delta_{\rm t}} D_{\rm vx} d\delta}_{\substack{\text{virtual damping} \\ \text{energy}}} \tag{30}$$

where δ_0 is the initial EPA and $\delta_{\rm t}$ is the EPA at any subsequent time t.

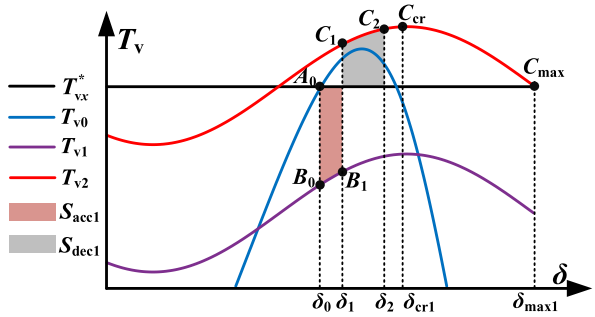

Fig. 6. Trajectory of the system operating point from prefault to fault duration stages.

In (30), the virtual potential energy represents the accumulation of the imbalance torque on EPA. The virtual kinetic energy represents the change in $\omega_{\rm PLL}$ equipment relative to $\omega_{\rm g}$. When EPA is within $[\delta_{\rm cr1}, \delta_{\rm cr2}]$, shown in Fig. 5(c), the virtual damping energy represents the energy loss of the VSC system in the EPA variation. However, virtual damping energy represents the energy accumulation caused by the negative $D_{\rm vx}$ when EPA runs in the range of $[\delta_{\min}, \delta_{\rm cr1}]$ and $[\delta_{\rm cr2}, \delta_{\max}]$, as shown in Fig. 5(c).

According to (21) and (30), the energy conversion relationship during the full grid fault process can be described by the trajectory of system operating points.

1) From Prefault to Fault Duration Stages: The trajectory of the system operating point from prefault to fault duration stages is shown in Fig. 6.

$A_0 \rightarrow B_0$: Assuming that the VSC system steadily runs at point A_0 during the prefault stage, which means $T_{\rm v0}^* = T_{\rm v0}$, and the corresponding EPA and $\omega_{\rm PLL}$ are δ_0 and $\omega_{\rm g}$, respectively. The operating point would instantaneously migrate to B_0 once the VSC system enters the fault dead-time stage. However, EPA and $\omega_{\rm PLL}$ do not change.

$B_0 \rightarrow B_1$: $T_{\rm v1}^* > T_{\rm v1}$ at point B_0, driven by excess $T_{\rm v1}^*$, $\omega_{\rm PLL}$ will gradually increase. Correspondingly, the EPA increases from δ_0 to δ_1. It is evident that there is no intersection between the curves of $T_{\rm v1}^*$ and $T_{\rm v1}$, which means that $\omega_{\rm PLL}$ will continue increasing if the fault dead-time stage lasts too long. The released virtual potential energy during this process can be illustrated as the accelerating area $S_{\rm acc1}$ shown in Fig. 6, which is calculated as

$$S_{\rm acc1} = \int_{\delta_0}^{\delta_1} (T_{\rm v1}^* - T_{v1}) d\delta. \tag{31}$$

$B_1 \rightarrow C_1$: LVRT strategy is switched in at point B_1, the curve of virtual output torque turns to $T_{\rm v2}$, and the operating point instantaneously migrates to point C_1.

$C_1 \rightarrow C_2$: $\omega_{\rm PLL} > \omega_{\rm g}$ at point C_1 although $T_{\rm v2}^* < T_{\rm v2}$. Consequently, the shortage of $T_{\rm v2}^*$ will result in a decrease of $\omega_{\rm PLL}$ and increase of EPA. Assuming that $\omega_{\rm PLL}$ decreases to $\omega_{\rm g}$ at point C_2, the EPA will stop increasing. The accumulated virtual potential energy during this process is illustrated as the decelerating area $S_{\rm dec1}$ shown in Fig. 6, which is calculated as

$$S_{\rm dec1} = \int_{\delta_1}^{\delta_2} (T_{v2} - T_{\rm v2}^*) d\delta. \tag{32}$$

The virtual energy conversion relationship from the prefault to the fault duration stage can be expressed as

$$\begin{cases} \Delta S_{\mathrm{DI}} = \frac{1}{\omega_{\mathrm{b}}} \int_{\delta_0}^{\delta_1} D_{v1} d\delta + \frac{1}{\omega_{\mathrm{b}}} \int_{\delta_1}^{\delta_2} D_{v2} d\delta \\ S_{\mathrm{acc1}} = S_{\mathrm{dec1}} + \Delta S_{\mathrm{DI}} \end{cases} \tag{33}$$

where ΔS_{DI} represents the virtual damping energy from the prefault stage to the fault duration stage. As shown in Fig. 6, D_{v2} is a positive value before EPA exceeds δ_{cr1}, and it is evident that the positive damping term could consume a part of the released virtual potential energy, thus promoting ω_{PLL} to converge to ω_{g}. However, D_{v2} becomes negative once the EPA exceeds δ_{cr1}.

Once EPA exceeds δ_{max1}, a transient synchronization instability occurs for the VSC system. Therefore, the following criterion shown is derived:

$$\begin{cases} \max(S_{\mathrm{dec1}}) = \int_{\delta_1}^{\delta_{\mathrm{max1}}} (T_{v2} - T_{\mathrm{v2}}^*) d\delta \\ \Delta S_{\mathrm{DI}} = \frac{1}{\omega_{\mathrm{b}}} \int_{\delta_0}^{\delta_1} D_{v1} d\delta + \frac{1}{\omega_{\mathrm{b}}} \int_{\delta_1}^{\delta_{\mathrm{max1}}} D_{v2} d\delta \\ S_{\mathrm{acc1}} \le \{\max(S_{\mathrm{dec1}}) + \Delta S_{\mathrm{DI}}\}. \end{cases} \tag{34}$$

Criterion (34) indicates that the released virtual potential energy during the fault dead-time stage must be completely consumed during the fault duration stage before EPA reaches δ_{max1}. Otherwise, the excess virtual energy will drive the system to exceed its transient stability limit, and thus, the ω_{PLL} will not return to ω_{g} and the LOS phenomenon for angular frequency increase will occur. Based on criterion (34), the critical clearing angle $\delta^{\mathrm{cut}}{}_{\mathrm{cr}}$ can be deduced as

$$\delta_{cr}^{cut} = \frac{(\omega_{\mathrm{g}} L_{\mathrm{g}} I_{\mathrm{dm}} + \frac{L_{\mathrm{g}} I_{\mathrm{dm}}}{\omega_{\mathrm{b}}})\delta_0 - (\omega_{\mathrm{g}} L_{\mathrm{g}} I_{\mathrm{df}}^* + R_{\mathrm{g}} I_{\mathrm{qf}}^* + \frac{L_{\mathrm{g}} I_{\mathrm{df}}^*}{\omega_{\mathrm{b}}})\delta_{\mathrm{max1}}}{\omega_{\mathrm{g}} L_{\mathrm{g}} I_{\mathrm{dm}} - \omega_{\mathrm{g}} L_{\mathrm{g}} I_{\mathrm{df}}^* - R_{\mathrm{g}} I_{\mathrm{qf}}^* + \frac{L_{\mathrm{g}} I_{\mathrm{dm}}}{\omega_{\mathrm{b}}} - \frac{L_{\mathrm{g}} I_{\mathrm{df}}^*}{\omega_{\mathrm{b}}}} + \frac{U_{\mathrm{gf}}(\cos\delta_0 - \cos\delta_{\mathrm{max1}}) + \frac{k_{\mathrm{pp}} U_{\mathrm{gf}}}{k_{\mathrm{ip}}}(\sin\delta_{\mathrm{max1}} - \sin\delta_0)}{\omega_{\mathrm{g}} L_{\mathrm{g}} I_{\mathrm{dm}} - \omega_{\mathrm{g}} L_{\mathrm{g}} I_{\mathrm{df}}^* - R_{\mathrm{g}} I_{\mathrm{qf}}^* + \frac{L_{\mathrm{g}} I_{\mathrm{dm}}}{\omega_{\mathrm{b}}} - \frac{L_{\mathrm{g}} I_{\mathrm{df}}^*}{\omega_{\mathrm{b}}}}. \tag{35}$$

Equation (35) implies that δ_0, R_{g}, L_{g}, LVRT current instruction, and PLL control parameters affect δ_{cr}^{cut}. Furthermore, the relationship between δ_{cr}^{cut} and the critical clearing time t_{cr}^{cut} is given as

$$t_{cr}^{cut} = (\delta_{cr}^{cut} - \delta_0) \sqrt{\frac{2J_{\mathrm{v1}}}{\omega_{\mathrm{b}}(S_{\mathrm{acc1}} - \Delta S_{\mathrm{DI}})}}. \tag{36}$$

Criterion (36) means that the detection delay in the fault dead-time stage cannot exceed t_{cr}^{cut}, which is equivalent to criterion (34). In addition, criterion (36) shows that smaller δ_0, larger δ_{cr}^{cut}, larger J_{v1}, and larger ΔS_{DI} could increase t_{cr}^{cut}, which is also beneficial to the transient synchronization stability of REG systems.

2) During Fault Duration Stage: When the accumulated virtual kinetic energy is completely consumed at point C_2, the trajectory of the system operating point during fault duration stage will run along the curve of T_{v2}. Thus, the synchronization process, illustrated in Fig. 7, can be analyzed as follows.

$C_2 \rightarrow C_{\mathrm{k}}$: $T_{\mathrm{v2}}^* < T_{\mathrm{v2}}$ during this process. The shortage of T_{v2}^* drives ω_{PLL} to continue decreasing. Correspondingly, the EPA decreases from δ_2 to δ_{k} and the imbalance virtual torque reduces until $T_{\mathrm{v2}}^* = T_{\mathrm{v2}}$. The equivalent decelerating area S_{dec2} shown

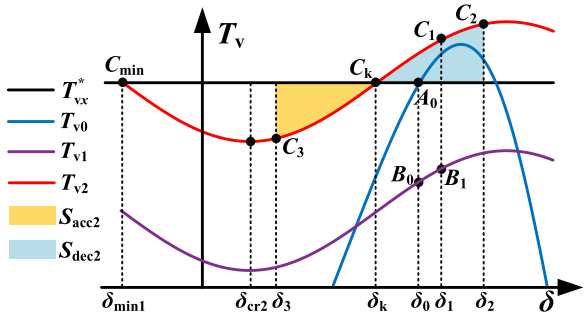

Fig. 7. Trajectory of the system operating point during fault duration stage.

in Fig. 7 is calculated as

$$S_{\mathrm{dec2}} = \int_{\delta_{\mathrm{k}}}^{\delta_2} (T_{v2} - T_{\mathrm{v2}}^*) d\delta. \tag{37}$$

C_{k}: $T_{\mathrm{v}}^* 2 = T_{\mathrm{v2}}$ when the VSC system reaches point C_{k}, and ω_{PLL} reaches the minimum. However, because the virtual kinetic energy is overconsumed when the system operating point moves from C_2 to C_{k}, this causes $\omega_{\mathrm{PLL}} < \omega_{\mathrm{g}}$ at point C_{k}, which further results in instability of the VSC system at point C_{k}, although $T_{\mathrm{v2}}^* = T_{\mathrm{v2}}$. As a result, the EPA continues decreasing.

$C_{\mathrm{k}} \rightarrow C_3$: $T_{\mathrm{v2}}^* > T_{\mathrm{v2}}$ and $\omega_{\mathrm{PLL}} < \omega_{\mathrm{g}}$ during this process, the excess $T_{\mathrm{v}}^* 2$ drives ω_{PLL} back to ω_{g}. Therefore, ω_{PLL} starts increasing whereas EPA continues decreasing. Assuming that ω_{PLL} increases to ω_{g} at point C_3, the EPA will stop decreasing. The equivalent accelerating area S_{acc2} during this process, shown in Fig. 7, is also calculated as

$$S_{\mathrm{acc2}} = \int_{\delta_3}^{\delta_{\mathrm{k}}} (T_{\mathrm{v2}}^* - T_{v2}) d\delta. \tag{38}$$

Similar to (33), the virtual energy conversion relationship during fault duration stage can be expressed as

$$\begin{cases} \Delta S_{\mathrm{DII}} = \frac{1}{\omega_{\mathrm{b}}} \int_{\delta_3}^{\delta_2} D_{v2} d\delta \\ S_{\mathrm{dec2}} = S_{\mathrm{acc2}} + \Delta S_{\mathrm{DII}} \end{cases} \tag{39}$$

where ΔS_{DII} represents the virtual damping energy during fault duration stage. In addition, (39) shows that the positive damping term could consume a part of accumulated virtual potential energy before EPA reaches δ_{cr2}, thus promoting ω_{PLL} to restore to ω_{g}. However, the value of D_{v2} would become negative once the EPA crosses δ_{cr2}.

Similar to (34), transient synchronization instability occurs for the VSC system once EPA exceeds δ_{min1}. Therefore, there is another criterion given as

$$\begin{cases} \max(S_{\mathrm{acc2}}) = \int_{\delta\,\mathrm{min}\,1}^{\delta_2} (T_{\mathrm{v2}}^* - T_{v2}) d\delta \\ \Delta S_{\mathrm{DII}} = \frac{1}{\omega_{\mathrm{b}}} \int_{\delta\,\mathrm{min}\,1}^{\delta_2} D_{v2} d\delta \\ S_{\mathrm{dec2}} \le \{\max(S_{\mathrm{acc2}}) + \Delta S_{\mathrm{DII}}\}. \end{cases} \tag{40}$$

Criterion (40) means that the excessive release of virtual kinetic energy must be totally restored before the EPA crosses δ_{min1}. Otherwise, the system will exceed its transient stability limit due to the shortage of the virtual kinetic energy, thus, the ω_{PLL} will not return to ω_{g} and the LOS phenomenon for angular frequency decrease will occur.

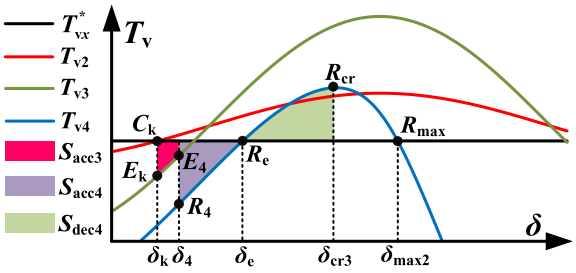

Fig. 8. Trajectory of the system operating point from the end of the fault duration stage to the postfault stage.

3) From the End of Fault Duration Stage to Postfault Stage: When criterions (34) and (40) are met, the VSC system can finally stabilize at point C_k during fault duration stage. However, the clearing of the grid fault would cause the system operation to change again. The trajectory of the system operating point from the end of the fault duration stage to the postfault stage is shown in Fig. 8.

Similar to the previous analysis, the VSC system will instantly enter fault recovery dead-time stage when the grid fault is cleared, such that the system operating point will migrate to point E_k from point C_k and then run along the curve of T_{v3}, as shown in Fig. 8.

When the restored grid voltage is detected at point E_4, the unit power factor operation mode is triggered again. Thus, the system operating point migrates to point R_4 from point E_4 and then runs along the curve of T_{v4}, on which the point R_e is the desired equilibrium point of the system during postfault stage.

The equivalent accelerating areas S_{acc3} and S_{acc4} from the end of the fault duration stage to the postfault stage are shown in Fig. 8. They are calculated as

$$\begin{cases} S_{acc3} = \int_{\delta_k}^{\delta_4} (T_{v3}^* - T_{v3}) d\delta \\ S_{acc4} = \int_{\delta_4}^{\delta_e} (T_{v4}^* - T_{v4}) d\delta. \end{cases} \tag{41}$$

In addition, the maximum value of S_{dec4} and the corresponding virtual damping energy ΔS_{DIII} are given as

$$\begin{cases} \max(S_{dec4}) = \int_{\delta_e}^{\delta_{max2}} (T_{v4} - T_{v4}^*) d\delta \\ \Delta S_{DIII} = \frac{1}{\omega_b} \int_{\delta_k}^{\delta_4} D_{v3} d\delta + \frac{1}{\omega_b} \int_{\delta_4}^{\delta_{max2}} D_{v4} d\delta. \end{cases} \tag{42}$$

Similar to criteria (34) and (40), the synchronization stability criterion of VSC system from the end of the fault duration stage to the postfault stage is given as

$$(S_{acc3} + S_{acc4}) \le \{\max(S_{dec4}) + \Delta S_{DIII}\}. \tag{43}$$

According to the analysis results in Part A of Section III, both the D_{v3} and D_{v4} are restored to a high level, such that ΔS_{DIII} could significantly consume virtual potential energy and virtual kinetic energy before EPA exceeds δ_{cr3}, which can help the VSC to avoid LOS instability phenomenon.

Combining Table I, criteria (34), (40), and (43), a considerable amount of d-axis current instruction will cause the curves of T_{vx} to move down, thus resulting in a decreasing of the maximum deceleration area. On the contrary, considerable q-axis current instruction will cause the curves of T_{vx} to move up, thus resulting in the decreasing of the maximum acceleration area. However, either the shortage of the maximum acceleration area or maximum deceleration area will result in the imbalanced virtual potential energy, and virtual kinetic energy will not be completely converted before the system reaches its transient synchronization stability limits. Consequently, the instruction setting significantly affects VSC system synchronization stability in the entire grid fault process.

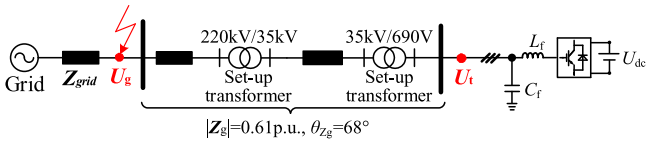

Fig. 9. Simulation configuration of the grid-connected VSC system.

The accumulation of the imbalanced virtual energy can be decreased by setting appropriate d/q-axis current instructions, thus improving the system synchronization stability. In addition, high and positive D_{vx} is also beneficial to consuming the imbalanced virtual energy, which can improve the synchronization stability.

VI. Simulation and Experiment Validation

A. Simulation Validation

To verify the previous analysis, the simulations on the 2 MW grid-connected VSC system were performed using MATLAB/Simulink. The simulated system was configured, as shown in Fig. 9. The main parameters of the simulation are given in Table I of the Appendix. Before the symmetrical fault occurs, $P_{pre}^* = 1.0$ p.u. The symmetrical grid fault occurs at 0.1 s, the grid voltage decreases to 0.3 p.u., and then the grid fault is cleared at 0.6 s.

Fig. 10 shows two simulation cases with the same operation condition but different fault detection delays.

The VSC system runs in a steady state during the prefault stage, which can be seen from Fig. 10(a)–(c). However, when symmetrical grid fault occurs because of the detection delay, the VSC system enters the fault dead-time stage and turns into a saturated current source, which is shown in Fig. 10(h) and (i) and is in agreement with (13). Furthermore, the increasing d-axis current will cause an increasing of U_{tq}, thus causing a decrease in T_{v1}, which means $T_{v1}^* > T_{v1}$, as shown in Fig. 10(e). Consequently, the excess T_{v1}^* drives ω_{PLL} to gradually increase, and the EPA increases before the LVRT strategy is triggered, which can be seen from Fig. 10(a) and (b).

When the VSC system enters the fault duration stage, the LVRT strategy is triggered, and LVRT instructions I_{qf}^* and I_{df}^* are set as –0.9 and 0.5 p.u., respectively, which can be seen from Fig. 10(h) and (j). From (20), there is a theoretical equilibrium point for the VSC system during the fault duration period under such condition. When the detection delay time is 5 ms in Case 1, the VSC system satisfies criterion (34) and the system stabilizes. However, when the detection delay time is 10 ms in Case 2, the VSC system does not satisfy criterion (34). As a result, the excess virtual energy causes the LOS phenomenon for angular

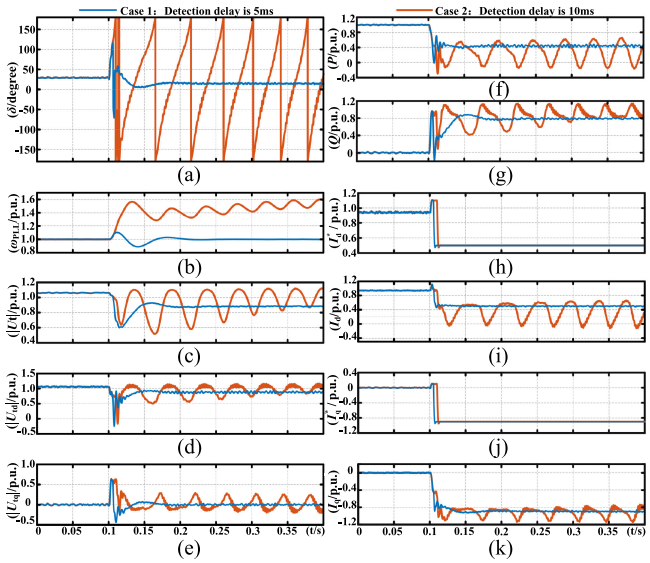

Fig. 10. Simulation results with different fault detection delays from prefault stage to fault duration stage. (a) EPA of system. (b) PLL's output angular frequency. (c) Amplitude of terminal voltage. (d) *d*-axis component of terminal voltage. (e) *q*-axis component of terminal voltage. (f) Output active power. (g) Output reactive power. (h) *d*-axis current instruction value. (i) Actual output *d*-axis current. (j) *q*-axis current instruction value. (k) Actual output *q*-axis current.

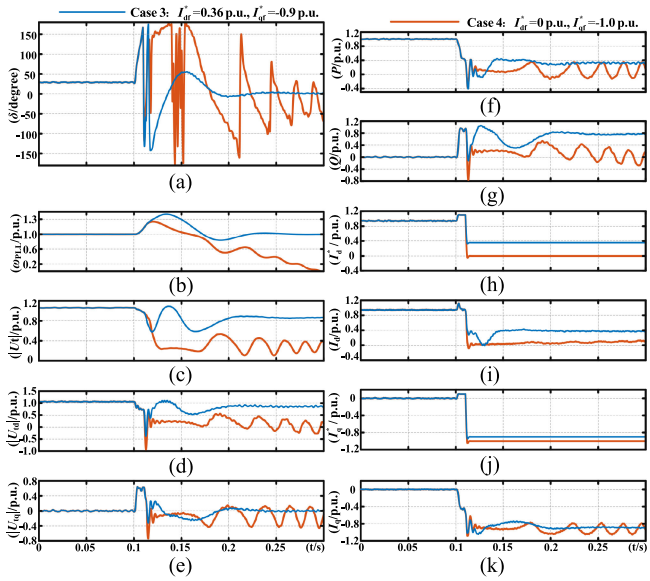

Fig. 11. Simulation cases with different *d*/*q*-axis current instructions during fault duration stage. (a) EPA of system. (b) PLL's output angular frequency. (c) Amplitude of terminal voltage. (d) *d*-axis component of terminal voltage. (e) *q*-axis component of terminal voltage. (f) Output active power. (g) Output reactive power. (h) *d*-axis current instruction value. (i) Actual output *d*-axis current. (j) *q*-axis current instruction value. (k) Actual output *q*-axis current.

frequency increase. All the simulation results in Fig. 10 are in agreement with the analysis result.

Fig. 11 shows two simulation cases with the same operation state during the prefault period and same fault detection delay time, but different LVRT instructions during fault duration period.

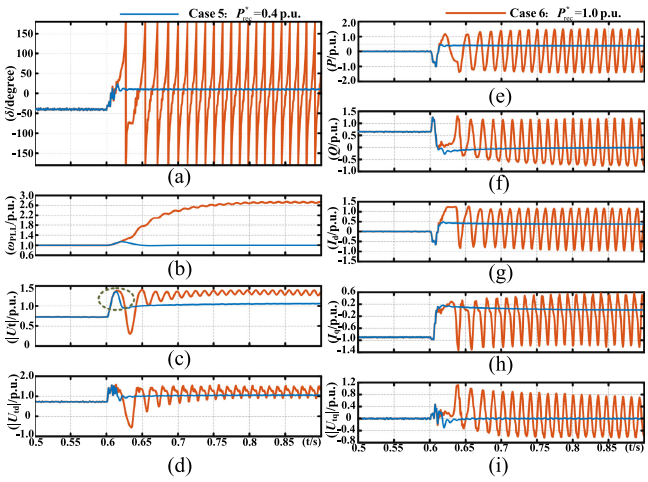

Fig. 12. Simulation cases with different active power instructions during postfault stage. (a) EPA of system. (b) PLL's output angular frequency. (c) Amplitude of terminal voltage. (d) *d*-axis component of terminal voltage. (e) Output active power. (f) Output reactive power. (g) Actual output *d*-axis current. (h) Actual output *q*-axis current. (i) *q*-axis component of terminal voltage.

I_{qf}^* and I_{df}^* of Case 3 are set as –0.9 and 0.36 p.u., respectively. I_{df}^* in Case 3 is smaller than that in Case 2, thus resulting in an increasing of the maximum deceleration area [max(S_{dec1})] according to (34). The increased maximum deceleration area could make the VSC system in Case 3 satisfy the criterion (34), thus the LOS phenomenon for angular frequency increase can be avoided. In addition, the VSC system in Case 3 also satisfies the criterion (40), and it can be finally stabilized after a severe transient synchronization process.

When I_{qf}^* and I_{df}^* of Case 4 are set as –1.0 and 0 p.u., respectively, a lower I_{df}^* and higher I_{qf}^* will decrease the acceleration area [max(S_{acc2})]. That is, the VSC system does not satisfy the criterion (40) although the criterion (34) is satisfied. Similar to the analysis result of (2) in Section V-B, the shortage of the virtual kinetic energy will lead to a continuous decrease in ω_{PLL} and the LOS phenomenon for angular frequency decrease will occur, which can be seen in Fig. 11(b).

Fig. 12 shows two simulation cases with the same operation state during fault duration stage and fault detection delay, but different active power instructions during postfault stage.

In Cases 5 and 6, I_{qf}^* and I_{df}^* of the VSC system during LVRT are –0.9 and 0 p.u., respectively. The VSC system enters the fault recovery dead-time stage when gird fault is cleared. Then, the VSC system enters the postfault stage after a detection delay of 5 ms, and P^*_{rec} is set as 0.4 p.u. in Case 5 and 1.0 p.u. in Case 6.

As can be seen from Fig. 12(c), the detection delay results in the reactive current instruction cannot be timely reduced, which causes the transient overvoltage phenomenon. Moreover, the restored grid voltage can considerably improve the value of VSC's virtual damping coefficient, such that the D_{v3} becomes higher than D_{v2}. As a result, the damping energy loss ΔS_{DIII} can significantly consume virtual potential energy and virtual kinetic energy, such that the transient synchronization process of ω_{PLL} and EPA from fault duration stage to postfault stage

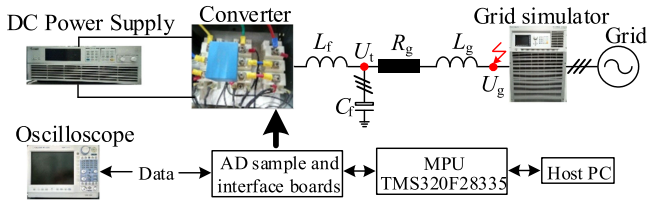

Fig. 13. Configuration of the grid-connected VSC system.

in Case 5 is not severe, as shown in Fig. 12(a) and (b). However, the considerable active power instruction is set on Case 6 during the postfault stage, and thus, the VSC system does not satisfy criterion (43). Consequently, the LOS phenomenon for angular frequency increase occurs. The simulation results are in agreement with the analysis results. The detailed virtual energy calculation verification for the simulation cases is given in Tables III, IV, and V of the Appendix.

B. Experimental Validation

To validate the analytical results, the structure of the laboratory-scale 2.0 kW grid-connected VSC system and its detailed experiment set up were configured, as in Fig. 13, in which the VSC was fed by a dc voltage source and controlled by TMS320F28335. In addition, there was a grid simulator using Chroma 61830, and three phase transmission lines emulated using reactors and oscilloscopes to measure data. The main parameters of the experiment are given in Table II of the Appendix. Using the grid simulator, the short-circuit fault occurred at 0.5 s and was cleared at 1.5 s.

Fig. 14 shows two experimental cases with the same operation state but different fault detection delays. As can be seen from Fig. 14 (a) and (b), $P^*_{\rm pre} = 1.0$ p.u. before the symmetrical fault occurs, and grid voltage decreases to 0.15 p.u. at 0.5 s. $I^*_{\rm df}$ and $I^*_{\rm qf}$ during LVRT are set as 0 and –1.0 p.u., respectively.

When the detection delay time is 15 ms in Experimental Case 1, the VSC system satisfies criterion (34), and, thus, stabilizes, which is shown in Fig. 14(a). However, when the detection delay time is 20 ms in Experimental Case 2, the longer detection delay time causes the LOS phenomenon responsible for angular frequency increase, which is shown in Fig. 14(b). In addition, when the grid fault is cleared at 1.5 s, the reactive current instruction cannot be reduced in time, which causes the transient overvoltage phenomenon shown in Fig. 14(a).

If $P^*_{\rm pre} = 0.5$ p.u. before the symmetrical fault occurs, then the grid voltage decreases to 0.1 p.u. at 0.5 s, and $I^*_{\rm qf}$ and $I^*_{\rm df}$ of Experimental Case 3 are set as –0.9 and 0 p.u., respectively, during LVRT. Thus, the VSC system does not satisfy criterion (40) although criterion (34) is satisfied. As a result, the shortage reduction of the virtual kinetic energy leads to a continuous decrease of $\omega_{\rm PLL}$ and the LOS phenomenon for angular frequency decrease occurs. The experimental result is given in Fig. 15(a).

If $I^*_{\rm qf}$ and $I^*_{\rm df}$ of Experimental Case 4 are still set as –0.9 and 0 p.u., respectively, during LVRT, but PLL's $k_{\rm ip}$ decreases from

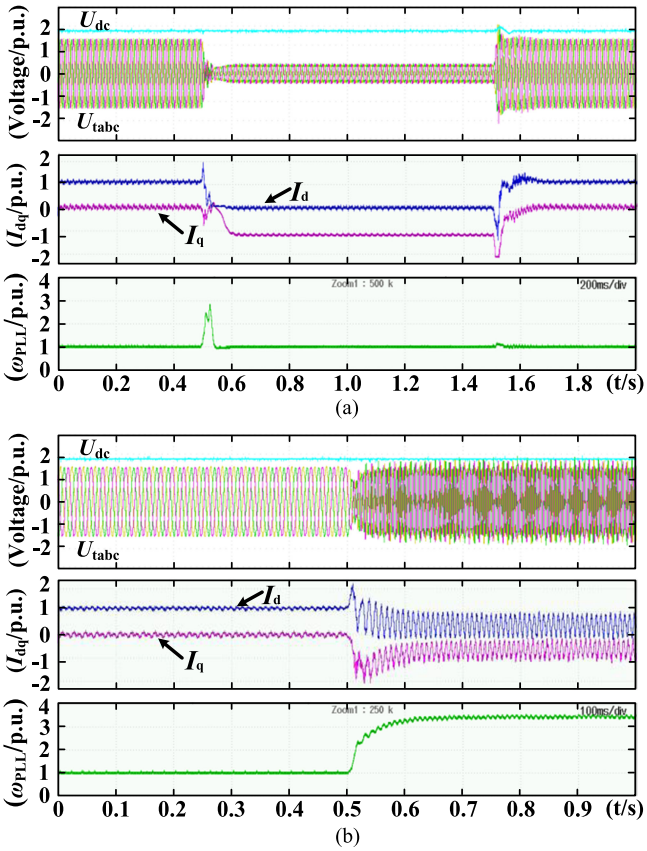

Fig. 14. Experimental results with different fault detection delays from prefault stage to fault duration stage. (a) Experimental Case 1: fault detection delay is approximately 15 ms. (b) Experimental Case 2: fault detection delay is approximately 20 ms.

80 to 10, the virtual damping coefficient of VSC system increases and consumes the imbalanced virtual energy. As a result, the virtual damping energy ($\Delta S_{\rm DII}$) increases according to (40). Consequently, the synchronization stability is improved, LOS phenomenon does not occur, and corresponding experimental result is shown in Fig. 15(b).

In addition, if $I^*_{\rm qf}$ and $I^*_{\rm df}$ are set as –0.9 and 0.2 p.u., respectively, during LVRT but the control parameters remain unchanged, the experimental results will be, as shown in Fig. 15(c). $I^*_{\rm df}$ of Experimental Case 5 is larger than that of Experimental Case 3, resulting in an increase of the maximum deceleration area [max($S_{\rm dec1}$)] according to (32). The increased maximum deceleration area enables the VSC system to satisfy criterion (40), thus, the LOS phenomenon for angular frequency increase can be avoided. Consequently, the VSC system can be finally stabilized after a transient synchronization process. Furthermore, it can be seen from Fig. 15(c) that an appropriate proportion of *d*/*q*-axis current can avoid LOS and the transient overvoltage phenomena when the grid fault is cleared.

The detailed virtual energy calculation verification of the experimental cases is provided in Tables VI, VII, and VIII of the Appendix.

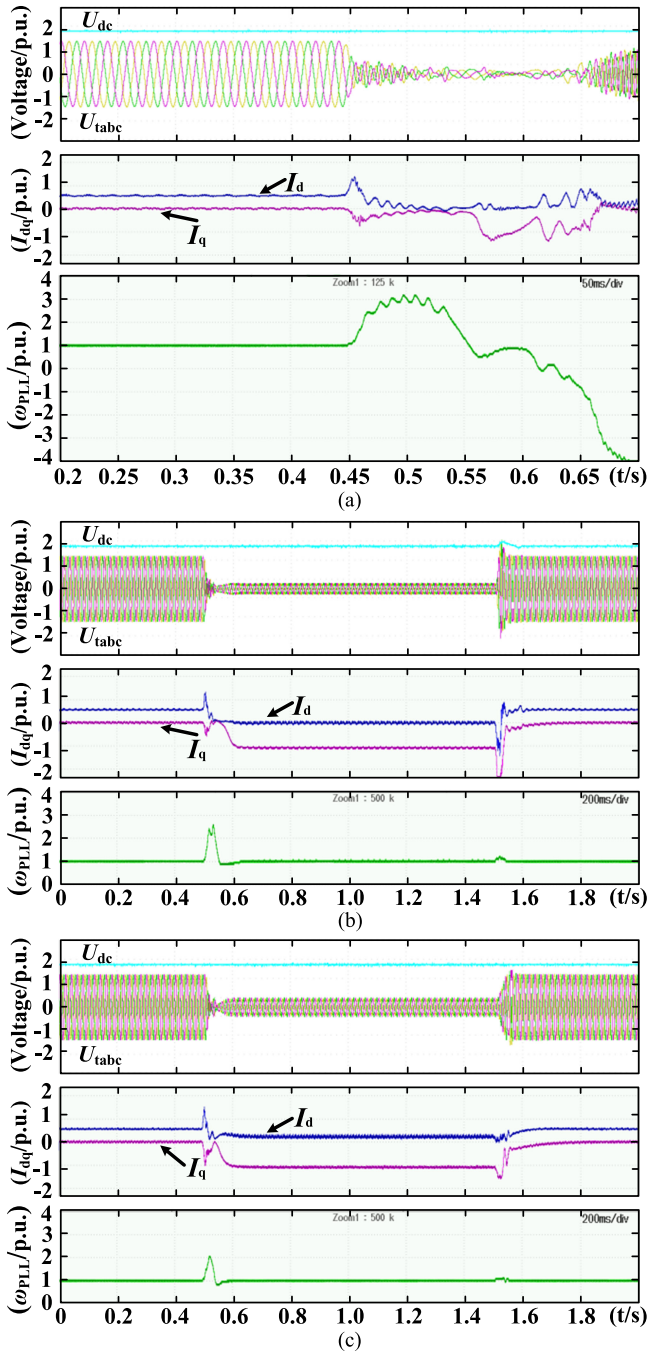

Fig. 15. Experimental results with different k_{ip} or different *d*/*q*-axis current instructions during fault duration stage. (a) Experimental Case 3: I^*_{qf} = -0.9 p.u., $I^*_{df} = 0$ p.u., and $k_{ip} = 80$. (b) Experimental Case 4: I^*_{qf} = –0.9 p.u., $I^*_{df} = 0$ p.u., and $k_{ip} = 10$. (c) Experimental Case 5: I^*_{qf} = –0.9 p.u., $I^*_{df} = 0.2$ p.u., and $k_{ip} = 80$.

VII. Conclusion

The transient model and synchronization stability of the PLL-based REG system was systematically analyzed in this article from the perspective of the entire grid fault process. The main analysis results are summarized as follows.

1) The transient synchronization mechanism of the PLL-based REG system for the different fault processes is expressed by the equivalent rotor swing equations, as is the case for SGs. Therefore, the transient synchronization characteristics of the REG system can be characterized by the deduced synchronous characteristic indexes, involving T^*_{vx}, T_{vx}, J_{vx}, D_{vx}, δ_{cr}, δ_{min}, δ_{max}, and t^{cut}_{cr}. In addition, the sequential control switching schemes of the REG system result in a change of system's transient synchronization characteristics.
2) The proposed EAC shows that the transient behaviors of the REG system during the entire grid fault process can be represented by the accumulation and release of imbalanced virtual energy. Consequently, the energy mismatch between the accumulated and the released virtual energy may lead to the LOS phenomenon. In addition, the sequential control switching schemes of the REG system affect the variation of imbalanced virtual energy. Based on the abovementioned considerations, criteria (34), (40), and (43) can completely evaluate LOS risk of the REG system for the entire grid fault process, which is also detailed as follows.
   a) The detection delay leads to an increase of the virtual potential energy of the REG system during fault dead-time stage, and thus may result in the LOS phenomenon for angular frequency increase. Moreover, with the detection delay, the reactive current instruction cannot be reduced in time when grid fault is cleared, which may cause the transient overvoltage phenomenon.
   b) During LVRT, the dominated injection of *q*-axis current may lead to excessive release of virtual kinetic energy of the REG system, thus causing the LOS phenomenon for angular frequency decrease. On the contrary, the dominated injection of *d*-axis current may cause the LOS phenomenon for angular frequency increase.
   c) During the postfault stage, the considerable active power instruction during the postfault stage increases the accumulation of virtual potential energy, which may theoretically lead to the LOS phenomenon after grid fault is cleared. The grid codes can strictly limit the active power instruction during postfault stage, which is beneficial for the REG system to achieve resynchronization with the power grid during the postfault stage.
3) Analysis results also revealed the coupled driving relationship between the angular frequency and terminal voltage of the REG system. As a consequence, the synchronization behaviors of REG's terminal angular frequency are driven by its terminal voltage, but the deviation of the REG's terminal angular frequency affects the terminal voltage. This interaction between the terminal angular frequency and terminal voltage provides the voltage-frequency coupled synchronization property for the REG system.

APPENDIX

TABLE II
PARAMETERS OF THE SIMULATION SYSTEM

Symbol	Description	Value (p.u.)
P_n	Rate power	1.5 MW (1 p.u.)
V_n	Rate voltage	690 V (1 p.u.)
V_{dc}	dc-link voltage	1200 V
f_g	Rate frequency	50 Hz
L_f	Grid-side filter inductance	0.25 p.u.
C_f	Filter capacitor	0.15 p.u.
k_{pp}, k_{ip}	PI gains of the PLL	1.0, 60
k_{pc}, k_{ic}	Current controller's PI parameters	2.5, 15
k_{pg}, k_{ig}	Power controller's PI parameters	1.0, 20

TABLE III
PARAMETERS OF THE EXPERIMENTAL SYSTEM

Symbol	Description	Value (p.u.)
P_n	Rate power	2.0 kW (1 p.u.)
V_n	Rate voltage	220 V (1 p.u.)
V_{dc}	dc-link voltage	430 V
f_g	Rate frequency	50 Hz (1 p.u.)
L_f	Grid-side filter inductance	5mH
C_f	Filter capacitor	30μF
R_g	Transmission line resistance	1.65 Ω
L_g	Transmission line inductance	21 mH
k_{pp}, k_{ip}	PI gains of the PLL	0.8, 80
k_{pc}, k_{ic}	Current controller's PI parameters	1.4, 0.4
k_{pg}, k_{ig}	Power controller's PI parameters	0.5, 0.02
T	Control period	400μs

TABLE IV
SIMULATION VERIFICATION OF CRITERION (34)

Simulation	f_{cr}^{cut}	Detection delay	Meet criterion (34)	Stability
Case 1	8.2ms	5ms	Yes	Stable
Case 2	**8.2ms**	**10ms**	**No**	**LOS**
Case 3	10.3 ms	10ms	Yes	Stable
Case 4	12.7ms	10ms	Yes	Stable

TABLE V
SIMULATION VERIFICATION OF CRITERION (40)

Simulation	S_{dec2}	$\max(S_{acc2})+\Delta S_{DII}$	Meet criterion (40)	Stability
Case 3	0.5613	0.5925	Yes	Stable
Case 4	**0.9636**	**0.0750**	**No**	**LOS**

TABLE VI
SIMULATION VERIFICATION OF CRITERION (43)

Simulation	$S_{acc3}+S_{acc4}$	$\max(S_{dec3})+\Delta S_{DIII}$	Meet criterion (43)	Stability
Case 5	0.351	0.5275	Yes	Stable
Case 6	**0.4905**	**0.0998**	**No**	**LOS**

TABLE VII
EXPERIMENTS VERIFICATION OF CRITERION (34)

Experimental	f_{cr}^{cut}	Detection delay	Meet criterion (34)	Stability
Case 1	18.6ms	15ms	Yes	Stable
Case 2	**18.6ms**	**20ms**	**No**	**LOS**
Case 3	16.8ms	10ms	Yes	Stable
Case 4	47.7ms	10ms	Yes	Stable
Case 5	14.9ms	10ms	Yes	Stable

TABLE VIII
EXPERIMENTS VERIFICATION OF CRITERION (40)

Experimental	S_{dec2}	$\max(S_{acc2})+\Delta S_{DII}$	Meet criterion (40)	Stability
Case 3	**0.3266**	**0.0447**	**No**	**LOS**
Case 4	0.0489	0.0511	Yes	Stable
Case 5	0.1290	0.1746	Yes	Stable

TABLE IX
EXPERIMENTS VERIFICATION OF CRITERION (43)

Experimental	$S_{acc3}+S_{acc4}$	$\max(S_{dec3})+\Delta S_{DIII}$	Meet criterion (43)	Stability
Case 1	0.1764	0.3615	Yes	Stable
Case 4	0.2783	0.6978	Yes	Stable
Case 5	0.0165	0.6381	Yes	Stable

REFERENCES

[1] A. K. Gupta, K. Verma, and K. R. Niazi, "Dynamic impact analysis of DFIG-based wind turbine generators on low-frequency oscillations in power system," *IET Gener. Transmiss. Distrib.*, vol. 11, no. 18, pp. 4500–4510, Dec. 2017.

[2] X. Wang, M. G. Taul, H. Wu, Y. Liao, F. Blaabjerg, and L. Harnefors, "Grid-synchronization stability of converter-based resources—An overview," *IEEE Open J. Ind. Appl.*, vol. 1, pp. 115–134, Aug. 2020.

[3] H. Liu *et al.*, "Subsynchronous interaction between direct-drive PMSG based wind farms and weak AC networks," *IEEE Trans. Power Sys.*, vol. 32, no. 6, pp. 4708–4720, Nov. 2017.

[4] B. Kroposki *et al.*, "Achieving a 100% renewable grid: Operating electric power systems with extremely high levels of variable renewable energy," *IEEE Power Energy Mag.*, vol. 15, no. 2, pp. 61–73, Mar./Apr. 2017.

[5] X. Zou, D. Zhu, J. Hu, S. Zhou, and Y. Kang, "Mechanism analysis of the required rotor current and voltage for DFIG-based WTs to ride-through severe symmetrical grid faults," *IEEE Trans. Power Electron.*, vol. 33, no. 9, pp. 7300–7304, Sep. 2018.

[6] Technical Rule for Connecting Wind Farm to Power System, Chinese Standard: GB/T 19963-2011, China Electric Power Press, Beijing, China, 2011.

[7] E. ON. Netz. GmbH, Grid code - high and extra high voltage, Bayreuth, Germany, Apr. 2006. [Online]. Available: https://wenku.baidu.com/view/9ca75c8ecc22bcd126ff0c4b.html

[8] J. Hu, Y. Huang, D. Wang, H. Yuan, and X. Yuan, "Modeling of grid-connected DFIG-based wind turbines for DC-link voltage stability analysis," *IEEE Trans. Sustain. Energy.*, vol. 6, no. 4, pp. 1325–1336, Oct. 2015.

[9] Y. Chang, J. Hu, and X. Yuan, "Mechanism analysis of DFIG-Based wind turbine's fault current during LVRT with equivalent inductances," *IEEE J. Emerg. Sel. Topics Power Electron.*, vol. 8, no. 2, pp. 1515–1527, Jun. 2020.

[10] W. Li, P. Chao, X. Liang, D. Xu, and X. Jin, "An improved single-machine equivalent method of wind power plants by calibrating power recovery behaviors," *IEEE Trans. Power Syst.*, vol. 33, no. 4, pp. 4371–4381, Jul. 2018.

[11] X. Wang, J. Yao, J. Pei, P. Sun, H. Zhang, and R. Liu, "Analysis and damping control of small-signal oscillations for VSC connected to weak AC grid during LVRT," *IEEE Trans. Energy Convers.*, vol. 34, no. 3, pp. 1667–1676, Sep. 2019.

[12] J. Hu, B. Wang, W. Wang, H. Tang, Y. Chi, and Q. Hu, "Small signal dynamics of DFIG-based wind turbines during riding through symmetrical faults in weak AC grid," *IEEE Trans. Energy Convers.*, vol. 32, no. 2, pp. 720–730, Jun. 2017.

[13] P. Sun, J. Yao, R. Liu, J. Pei, H. Zhang, and Y. Liu, "Virtual capacitance control for improving dynamic stability of the DFIG-based wind turbines during a symmetrical fault in a weak AC grid," *IEEE Trans. Ind. Electron.*, vol. 68, no. 1, pp. 333–346, Jan. 2021.

[14] M. G. Taul, X. Wang, P. Davari, and F. Blaabjerg, "An overview of assessment methods for synchronization stability of grid-connected converters under severe symmetrical grid faults," *IEEE Trans. Power Electron.*, vol. 34, no. 19, pp. 9655–9670, Oct. 2019.

[15] Ö. Göksu, R. Teodorescu, C. L. Bak, F. Iov, and P. C. Kjær, "Instability of wind turbine converters during current injection to low voltage grid faults and PLL frequency based stability solution," *IEEE Trans. Power Syst.*, vol. 29, no. 4, pp. 1683–1691, Jul. 2014.

[16] D. Dong, B. Wen, D. Boroyevich, P. Mattavelli, and Y. Xue, "Analysis of phase-locked loop low-frequency stability in three-phase grid-connected power converters considering impedance interactions," *IEEE Trans. Ind. Electron.*, vol. 62, no. 1, pp. 310–321, Jan. 2015.
[17] J. Pei *et al.*, "Characteristic analysis and risk assessment for Voltage-frequency coupled transient instability of large-scale grid-connected renewable energy plants during LVRT," *IEEE Trans. Ind. Electron.*, vol. 67, no. 7, pp. 5515–5530, Jul. 2020.
[18] W. Tang, J. Hu, Y. Chang, and F. Liu, "Modeling of DFIG-based WT for power system transient response analysis in rotor speed control timescale," *IEEE Trans. Power Sys.*, vol. 33, no. 6, pp. 6795–6805, Nov. 2018.
[19] H. Geng, L. Liu, and R. Li, "Synchronization and reactive current support of PMSG-based wind farm during severe grid fault," *IEEE Trans. Sustain. Energy.*, vol. 9, no. 4, pp. 1596–1604, Oct. 2018.
[20] X. He, H. Geng, R. Li, and B. C. Pal, "Transient stability analysis and enhancement of renewable energy conversion system during LVRT," *IEEE Trans. Sustain. Energy.*, vol. 11, no. 3, pp. 1612–1623, Jul. 2020.
[21] H. Wu and X. Wang, "Design-oriented transient stability analysis of grid-connected converters with power synchronization control," *IEEE Trans. Ind. Electron.*, vol. 66, no. 8, pp. 6473–6482, Aug. 2019.
[22] H. Wu and X. Wang, "Transient stability impact of the phase-locked loop on grid-connected voltage source converters," in *Proc. Int. Power Electron. Conf.*, Niigata, 2018, pp. 2673–2680.
[23] ENTSO-E, "High penetration of power electronic interfaced power sources and the potential contribution of grid forming converters," Brussels, Belgium, Jan. 2020. [Online]. Available: https://eepublicdownloads.entsoe.eu/clean-documents/Publications/SOC/High_Penetration_of_Power_Electronic_Interfaced_Power_Sources_and_the_Potential_Contribution_of_Grid_Forming_Converters.pdf
[24] T. Qoria, F. Gruson, F. Colas, G. Denis, T. Prevost, and X. Guillaud, "Critical clearing time determination and enhancement of grid-forming converters embedding virtual impedance as current limitation algorithm," *IEEE J. Emerg. Sel. Topics Power Electron.*, vol. 8, no. 2, pp. 1050–1061, Jun. 2020.
[25] Y. Chang, J. Hu, W. Tang, and G. Song, "Fault current analysis of type-3 WTs considering sequential switching of internal control and protection circuits in multi time scales during LVRT," *IEEE Trans. Power Syst.*, vol. 33, no. 6, pp. 6894–6903, Nov. 2018.
[26] H. Yuan, H. Xin, L. Huang, Z. Wang, and D. Wu, "Stability analysis and enhancement of type-4 wind turbines connected to very weak grids under severe voltage sags," *IEEE Trans. Energy Convers.*, vol. 34, no. 2, pp. 838–848, Jun. 2019.
[27] D. Pérez-Estévez, J. Doval-Gandoy, A. G. Yepes, Ó. López, and F. Baneira, "Enhanced resonant current controller for grid-connected converters with LCL filter," *IEEE Trans. Power Electron.*, vol. 33, no. 5, pp. 3765–3778, May 2018.
[28] J. P. da Costa, H. Pinheiro, T. Degner, and G. Arnold, "Robust controller for DFIGs of grid-connected wind turbines," *IEEE Trans. Ind. Electron.*, vol. 58, no. 9, pp. 4023–4038, Sep. 2011.
[29] M. Rahimi and M. Parniani, "Efficient control scheme of wind turbines with doubly fed induction generators for low-voltage ride-through capability enhancement," *IET Renewable Power Gener.*, vol. 4, no. 3, pp. 242–252, May 2010.
[30] C. Ma, F. Gao, G. He, and G. Li, "A voltage detection method for the voltage ride-through operation of renewable energy generation systems under grid voltage distortion conditions," *IEEE Trans. Sustain. Energy*, vol. 6, no. 3, pp. 1131–1139, Jul. 2015.
[31] F. Xiao, L. Dong, L. Li, and X. Liao, "Fast voltage detection method for grid-tied renewable energy generation systems under distorted grid voltage conditions," *IET Power Electron.*, vol. 10, no. 12, pp. 1487–1493, Oct. 2017.

Jinxin Pei received the B.Eng. degree in electrical engineering and automation from Henan Polytechnic University, Jiaozuo, China, in 2016, and the Ph.D. degree from the College of Electrical Engineering, Chongqing University, Chongqing, China, in 2021.

His research interests include electric machines control, modeling and control of wind turbine generation system, and renewable power generation.

Jun Yao (Member, IEEE) received the B.Eng., M.Sc., and Ph.D. degrees from Chongqing University, Chongqing, China, in 2001, 2004, and 2007, respectively, all in electrical engineering.

Since 2004, he has been with the School of Electrical Engineering, Chongqing University, where he is currently a Professor. He was a Visiting Researcher with the Department of Energy Technology, Aalborg University, Aalborg, Denmark, from 2012 to 2013. He has authored/coauthored more than 80 peer-reviewed technical papers, and holds more than 20 issued/pending patents. His research interests include electric machines control, power electronics conversion and control, and renewable power generation; and his main current research interests include wind energy and power electronics application to the power systems.

Prof. Yao is a member of IEC SC8A JWG5.

Yuan Liu received the B.Eng. degree in electrical engineering and automation from China University of Mining and Technology, Xuzhou, China, in 2018, and the M.Sc. degree from the School of Electrical Engineering, Chongqing University, Chongqing, China, in 2021.

His research interests include electric machines control, and control of wind turbine generation system.

Shiyue Chen received the B.Eng. degree in electrical engineering and automation from Hefei University of Technology, Hefei, China, in 2019. She is currently working toward the M.Sc. degree in electrical engineering with the School of Electrical Engineering, Chongqing University, Chongqing, China.

Her research interests include power system transient analysis, and control of wind turbine generation system.

Peng Sun received the B.Eng. degree in electrical engineering and automation from Anhui University, Hefei, China, in 2017. He is currently working toward the Ph.D. degree with the School of Electrical Engineering, Chongqing University, Chongqing, China.

His research interests include electric machines control, modeling and control of wind turbine generation system, and renewable power generation.

Sen Huang received the B.Eng. degree in electrical engineering and automation from Northwest A&F University, Yangling, China, in 2019. He is currently working toward the Ph.D. degree with the College of Electrical Engineering, Chongqing University, Chongqing, China.

His research interests include electric machines control, modeling and control of wind turbine generation system, and renewable power generation.